Pseudo-Three-Layer Sequential Model-Free Predictive Control With Neural-Network Observer for Parallel T-Type Three-Level Converters

Tianxu Cao, *Student Member, IEEE*, YinHui Yu, Jiahao Zhang, Jose Rodriguez, *Life Fellow, IEEE*, Kil To Chong, *Member, IEEE*, and Bo Long, *Senior Member, IEEE*

***Abstract*—Parallel T-type three-level converter (3LT^{2}C) system has been widely concerned with its high-quality output current and improved efficiency in low-voltage applications. However, for parallel 3LT^{2}C, the power quality of the grid current should be considered, and the neutral-point (NP) voltage and zero-sequence circulating current (ZSCC) should be suppressed. In addition, the filter inductor mismatch can also seriously affect the overall performance. Based on the above considerations, this article proposes a novel sequential model-free predictive control method based on an ultralocal model (ULM) and a neural-network observer (NNO) for parallel-3LT^{2}C. First, a cost function-free NP voltage control is designed, which significantly suppresses the NP voltage fluctuations and does not need to know the values of dc-bus capacitances. Second, the ULMs of the grid-side current and ZSCC are designed, and the uncertain terms of the ULM are estimated with high accuracy by the NNO. Finally, a pseudo-three-layer sequential model predictive control is designed to simplify the weight factor selection. Comparative simulations and experiments verify the excellent performance of the proposed algorithm under parameter mismatch and different current references.**

***Index Terms*—Model-free predictive control (MFPC), neural-network observer (NNO), parallel three-level converters (3LT^{2}C), robustness, sequential model predictive control (SMPC), zero-sequence circulating current (ZSCC).**

Manuscript received 31 May 2023; revised 17 September 2023, 8 October 2023, 8 January 2024, and 10 February 2024; accepted 16 March 2024. Date of publication 20 March 2024; date of current version 16 May 2024. This work was supported in part by the Natural Science Foundation of Sichuan Province under Grant 23NSFSC0294, in part by Guangdong Basic and Applied Basic Research Foundation under Grant 2023A1515240058, and in part by the Funding for Chengdu Science and Technology Bureau level International Cooperation Projects under Grant 2023-GH02-00014-HZ. Recommended for publication by Associate Editor M. Narimani. *(Corresponding Author: Bo Long.)*

Tianxu Cao, Jiahao Zhang, and Bo Long are with the Yangtze Delta Region Institute (Huzhou), University of Electronic Science and Technology of China (UESTC), Huzhou 313001, China, also with the School of Mechanical and Electrical Engineering, University of Electronic Science and Technology of China, Chengdu 611731, China, and also with the Institute of Electronic and Information Engineering, University of Electronic Science and Technology of China, Guangdong 523808, China (e-mail: 202021040338@std.uestc.edu.cn; 202022040620@std.uestc.edu.cn; longbouestc1980@126.com).

YinHui Yu is with China Nuclear Power Technology Research Institute Company Ltd., Shenzhen 518100, China (e-mail: cqu_engineers@163.com).

Jose Rodriguez is with the Faculty of Engineering, Universidad Andres Bello, Santiago 8370146, Chile (e-mail: jose.rodriguezp@uss.cl).

Kil To Chong is with the Department of Electronics and Information Engineering, Jeonbuk National University, Jeonju 54896, South Korea (e-mail: kitchong@jbnu.ac.kr).

Color versions of one or more figures in this article are available at https://doi.org/10.1109/TPEL.2024.3379419.

Digital Object Identifier 10.1109/TPEL.2024.3379419

I. Introduction

PARALLEL three-level T-type converter (3LT^{2}C) system has drawn a lot of interest since the emergence of power electronic-based renewable energy systems because of its enhanced output current quality [1] and increased overall efficiency [2]. However, the parallel-3LT^{2}C system also includes at least two more control objectives in addition to the output current—the suppressions of the neutral-point (NP) voltage and zero-sequence circulating current (ZSCC). The former is caused by the unequal voltage distribution of two dc-bus side capacitors [3], whereas the latter is caused by the distinct common-mode voltages (CMVs) of different converters with different output current references and filter characteristics [4]. ZSCC inhibition techniques have been carefully examined recently [4], [5], [6], [7]. In [5], an interleaved discontinuous pulsewidth modulation (PWM) method for parallel two-level converters was proposed, which offers the lowest switching loss and eliminates the medium ZSCC change rates. In [6], a three-level converter carrier-based discontinuous PWM approach was put forth. This technique can be simply applied to parallel systems with NP voltage and ZSCC suppressions and decreases switching loss. In [7], it was suggested to use an integrated space-vector PWM (SVPWM) technique to reduce the CMV without compromising the grid current quality. When dealing with a parallel system, the modulation index and vector time distribution should be carefully considered, regardless of whether it utilizes PWM or SVPWM modulation technique, because they are required to ensure grid current quality, adequate ZSCC suppression, and NP voltage balance.

To achieve the multi-objective control of parallel-3LT^{2}C systems, finite-control-set model-predictive-control (FCS-MPC) has drawn much interest because of its benefits over conventional linear control. It offers many benefits, such as easy implementation, quick dynamic response, and no pulse-width modulation [8]. The control methods based on FCS-MPC applied in parallel three-level converters can be found in previous studies [9], [10], [11], which effectively eliminated the ZSCC by substituting candidate voltage vectors (CVVs) with low CMV values into the cost function, where all 27 CVVs were categorized according to their impacts on the CMV. In [11], virtual vectors (VVs) were employed to improve the current accuracy and expand the flexibility of ZSCC suppression. However, the aforementioned

ZSCC suppression techniques inadequately ensure ZSCC robustness when filter parameters are mismatched; this is a typical issue with FCS-MPC-based techniques.

Therefore, model-free predictive control (MFPC) has been widely advocated for increasing the robustness of FCS-MPC concerning filter parameter mismatch in power converter and drive systems [12], [13], [14], [15], [16], [17], [18], [19], [20], [21], [22], [23], [24]. A literature overview found that MFPC may be classified into three types as follows [25]:

1) Data-driven model [12], [13], [14]: This method does not require any system parameters, and the prediction is achieved only by sampling current values. A lookup table stores the variation of the sampled current corresponding to all CVVs. i.e., in [13], a data-driven model was implemented for a two-level inverter-fed permanent magnet synchronous motor (PMSM) with a current gradient updating mechanism. The results have shown good robustness and simple computation. In [14], the data-driven model for a three-level inverter-fed PMSM was designed. The appropriate selection of short vectors suppressed the NP voltage. However, the data-driven approach is not easy to achieve multiobjective control for parallel-3LT^{2}C because additional lookup tables and targeted update algorithms are required.
2) Prediction correction [15], [16]: This approach requires an accurate model of the system. Despite the parameter mismatch, the additional algorithm ensures that the filter parameters in the controller are close to their actual values. For example, in [15], a gradient descent algorithm was implemented to update parameter values. Apparently, the parameter correction module increases the computational burden.
3) Ultralocal model (ULM) [17], [18], [19], [20], [21], [22], [23], [24]: ULM recharacterizes the exact model with several certain and uncertain terms. The sensitivity to parameter changes is reduced by the estimation for uncertain terms. Standard uncertain term estimation algorithms include differential algebraic identification [17], extended state observer (ESO) [18], [19], etc. In [20], cascaded ESO was proposed to further improve the estimation accuracy and the anti-sampling noise ability. Moreover, in [21] and [22], a series of algorithms based on the neural-network observer (NNO) for modular multilevel converters were established, demonstrating better robustness and steady-state performance. For parallel three-level converters, the current study has successfully implemented the ULM-based MFPC method [23], [24]. For instance, in [24], ESO estimated the uncertain term of ULM, and VVs were used to increase the controllability of ZSCC. In conclusion, ULM-based MFPC has strong designability and portability compared to data-driven and prediction correction methods [25], thereby being adopted in this article.

In recent years, numerous researchers have extensively investigated the application of sequential model predictive control (SMPC) in motor control and other disciplines [26], [27], [28]. This method transforms the multi-objective optimization problem into several cascaded single-objective optimization problems and simplifies the selection of weights. In [29], [30], and [31], we systematically studied the improvement of SMPC in various three-level systems. Based on the original SMPC, we added two steps: simplification and reconstruction of finite-control-set (FCS). This design can significantly reduce the cycles of exhaustive calculation and trial time of weights. In [31], a simplified SMPC for parallel-3LT^{2}C was proposed, but ZSCC was suppressed by selecting CVVs that can suppress CMV. The robust design for ZSCC with the SMPC architecture has yet to be further investigated.

Therefore, in this article, a pseudo-three-layer sequential model-free predictive control (P3L-SMFPC) with NNO for the parallel-3LT^{2}C system was presented. The proposed method achieves excellent current quality and tracking ability with the NP voltage and ZSCC significantly inhibited under the filter parameter mismatch. Specifically, the followings are the main contributions of this article.

1) A novel NP voltage control method was proposed. The CVVs were selected based on the positive and negative values of the NP voltage and the grid-side currents. The selected CVVs can avoid the continuous increase or decrease of the NP voltage. Moreover, this method is insensitive to filter parameters and does not require the acquisition of dc-bus capacitances.
2) Robust control methods of grid-side currents and ZSCC are designed. The ULMs of grid-side currents and ZSCC were constructed, and NNO estimated the uncertain terms. Compared with the ESO in [18], this method presented lower current tracking errors with better robustness.
3) A pseudo-three-layer SMPC was designed. This structure retains all the advantages of the previous proposal in [31]. (i.e., fewer computation cycles and less trial time of weight factors.) Compared with traditional SMPC [26], [27], [28], this structure only needs to design one weighting factor, and its selection range is very narrow.

The rest of this article is organized as follows. Section II presents the prediction model for parallel-3LT^{2}Cs and analysis the robustness of FCS-MPC and SMPC. Section III proposes the NNO-based P3L-SMFPC method. Section IV examines the comparative simulation under filter parameter mismatch with different current references. Furtherly, experimental verifications are included in Section V. Finally, Section VI concludes the article.

II. Analysis for Parallel-3LT^{2}C

A. Prediction Model of the Parallel-3LT2C

The topology of the parallel-3LT2C system is demonstrated in Fig. 1. The two converters share the dc and ac buses, and the dc-bus side is composed of two series-connected capacitors C_1 and C_2, with voltages u_p and u_n, respectively. Each 3LT^{2}C is linked to a filter inductor L_1, and $R_1$is the parasitic resistance of L_1. v_i, i_1, i_g, and v_g are the converter-side voltage, grid-side current, point-of-common-coupling current, and grid voltage, respectively.

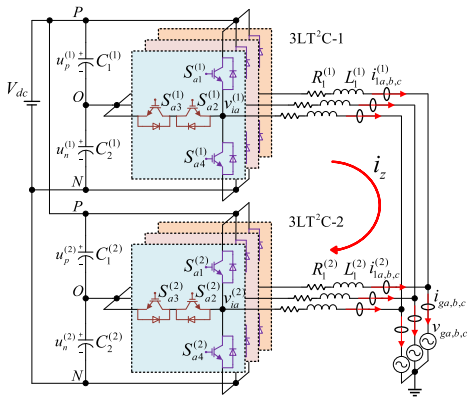

Fig. 1. Topology of the parallel-3LT^{2}C system.

A 3LT^{2}C features with 27 switching state combinations, which can be understood as the CVVs of FCS-MPC. The CVV can be described as

$$\begin{aligned}&\boldsymbol{u}^{(x)}=\left[u_a^{(x)},u_b^{(x)},u_c^{(x)}\right]^T\\&\text{s.t.}u_a,u_b,u_c\in\{-1,0,1\}x=1,2\end{aligned}\tag{1}$$

where $-1, 0$, and 1 represent the low-, medium-, and high voltage levels, respectively. (x) represents the number of converters, and the formula not marked with (x) is used for both converters unless otherwise specified.

Assuming a balanced NP voltage, the converter-side voltage can be stated as follows:

$$\boldsymbol{v}_i=\frac{V_{\text{dc}}}{2}\boldsymbol{u}\tag{2}$$

where $\boldsymbol{v}_i=[v_{ia},v_{ib},v_{ic}]^T$.

The parallel-3LT^{2}C system controls three variables: grid-side currents, NP voltage, and ZSCC. Their prediction models are discussed as follows.

First, according to Kirchhoff's law, the circuit equations for the grid-side currents were derived as

$$\begin{cases}\frac{di_{1a}}{\text{d}t}=-\frac{R_1}{L_1}i_{1a}-\frac{1}{L_1}v_{ga}+\frac{V_{\text{dc}}}{2L_1}u_a\\\frac{di_{1b}}{dt}=-\frac{R_1}{L_1}i_{1\text{b}}-\frac{1}{L_1}v_{gb}+\frac{V_{\text{dc}}}{2L_1}u_b\\\frac{di_{1c}}{dt}=-\frac{R_1}{L_1}i_{1c}-\frac{1}{L_1}v_{gc}+\frac{V_{\text{dc}}}{2L_1}u_c\end{cases}.\tag{3}$$

The discretized-time state equation of the grid-side currents of $\alpha\beta$ frame were obtained by discretizing (3) using the forward Euler method and Clarke transformations, as given as

$$\begin{aligned}\boldsymbol{i}_{1\alpha\beta}(k+1)=&\left(1-\frac{R_1T_s}{L_1}\right)\boldsymbol{i}_{1\alpha\beta}(k)-\frac{T_s}{L_1}\boldsymbol{v}_{g\alpha\beta}(k)\\&+\frac{V_{\text{dc}}T_s}{2L_1}\boldsymbol{C}_{3s/2s}\boldsymbol{u}(k)\end{aligned}\tag{4}$$

where $\boldsymbol{i}_{1\alpha\beta}=[i_{1\alpha},i_{1\beta}]^T$, $\boldsymbol{v}_{g\alpha\beta}=[v_{g\alpha},v_{g\beta}]^T$, $\boldsymbol{C}_{3s/2s}=\frac{2}{3}\begin{bmatrix}1&-1/2&-1/2\\0&\sqrt{3}/2&-\sqrt{3}/2\end{bmatrix}$, and T_s represents the sampling interval.

Second, for $C_1=C_2$, the NP voltage can be defined as

$$u_{\text{np}}=u_n-u_p.\tag{5}$$

Therefore, using Kirchhoff's current law, the circuit equation for the NP voltage can be rewritten as follows:

$$\frac{du_{\text{np}}}{dt}=\frac{1}{C_1}|\boldsymbol{u}|^T\boldsymbol{i}_1\tag{6}$$

where $\boldsymbol{i}_1=[i_{1a},i_{1b},i_{1c}]^T$.

Using forward Euler discretization, the NP voltage during one switching period can be represented as follows:

$$u_{\text{np}}(k+1)=\frac{T_s}{C_1}|\boldsymbol{u}(k)|^T\boldsymbol{i}_1(k)+u_{\text{np}}(k).\tag{7}$$

Third, the ZSCC was defined as

$$i_z=i_z^{(1)}=\sum_{n=a,b,c}i_{1n}^{(1)}=-i_z^{(2)}=\sum_{n=a,b,c}i_{1n}^{(2)}.\tag{8}$$

According to Kirchhoff's current law, the equivalent circuit equation of ZSCC can be constructed as follows:

$$\left(L_1^{(1)}+L_1^{(2)}\right)\frac{di_z}{dt}+\left(R_1^{(1)}+R_1^{(2)}\right)i_z=3\left(u_{\text{cmv}}^{(2)}-u_{\text{cmv}}^{(1)}\right)\tag{9}$$

where

$$u_{\text{cmv}}=\frac{v_{ia}+v_{ib}+v_{ic}}{3}=\frac{V_{\text{dc}}}{6}\begin{bmatrix}1&1&1\end{bmatrix}\boldsymbol{u}\tag{10}$$

represents the CMV.

B. Robustness Comparison Between FCS-MPC and SMPC

According to the aforementioned equations of the three control variables, the cost function of FCS-MPC can be described as follows:

$$\begin{aligned}&J(k)=J_i(k)+\lambda_{\text{np}}J_{\text{np}}(k)+\lambda_{\text{cmv}}J_{\text{cmv}}(k)\\&=\left\|\left(1-\frac{R_1T_s}{L_1}\right)\boldsymbol{i}_{1\alpha\beta}(k)-\frac{T_s}{L_1}\boldsymbol{v}_{g\alpha\beta}(k)\right.\\&\quad\left.+\frac{V_{\text{dc}}T_s}{2L_1}\boldsymbol{C}_{3s/2s}\boldsymbol{u}(k)-\boldsymbol{i}_{1\text{ref}}(k+1)\right\|\\&\quad+\lambda_{\text{np}}\left|\frac{T_s}{C_1}|\boldsymbol{u}(k)|^T\boldsymbol{i}_1(k)+u_{\text{np}}(k)\right|+\lambda_{\text{cmv}}\left|u_{\text{cmv}}(k)\right|\end{aligned}\tag{11}$$

where J_i, J_{np}, and J_{cmv} are the cost functions of $\boldsymbol{i}_1$, u_{np}, and u_{cmv}, respectively. $\boldsymbol{i}_{1\text{ref}}=[i_{1\alpha\text{ref}},i_{1\beta\text{ref}}]^{\text{T}}$ represents the reference of $\boldsymbol{i}_1$. λ_{np}, and λ_{cmv} denote the weighting factors of J_{np} and J_{cmv}, respectively.

In (11), only J_i is related to L_1, while J_{np} and J_{cmv} are not. However, the weighted cost function calculates a globally optimal solution, thereby deteriorating the three control variables simultaneously when L_1 is mismatched.

The SMPC algorithm, on the other hand, can be represented as follows:

$$J_{\text{np}}(k)\overset{n_1\text{CVVs}}{\rightarrow}J_{\text{cmv}}(k)\overset{n_2\text{CVVs}}{\rightarrow}J_i(k)\rightarrow\boldsymbol{u}_{\text{opt}}(k)\tag{12}$$

where n_1 and n_2 represent the number of CVVs output by the first and second cost functions and are defined as the weighting numbers, and $\boldsymbol{u}_{\text{opt}}$ is the optimal solution.

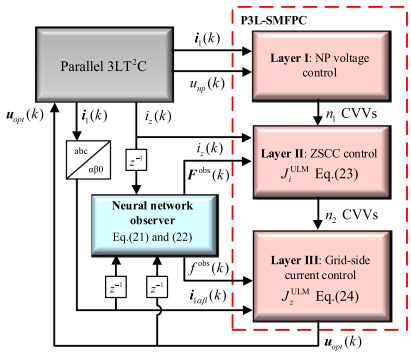

Fig. 2. Control flowchart of the proposed NNO-based P3L-SMFPC method.

It can be seen from (11) and (12) that the control of NP voltage ends when J_{np} calculates n_1 CVVs, and the same is true for J_{cmv}. In other words, CMV and NP voltage controlled by SMPC is independent of the variation of L_1. Therefore, compared with FCS-MPC with fixed weighting factors, SMPC can significantly reduce the coupling degree of the robustness of each control objective. This finding was verified in subsequent simulations and experiments.

Remark 1: ZSCC is commonly suppressed by directly controlling CMV to eliminate the excitation source of ZSCC [9], [10], [11]. However, it can be seen from (9) that L_1 and CMV jointly affect i_z, indicating that the sole regulation of CMV cannot adaptively inhibit ZSCC for a mismatched L_1. Therefore, to achieve the robustness of ZSCC, a ULM of ZSCC is constructed, and its uncertain term is estimated by NNO.

Remark 2: For SMPC, if J_i is located in the first layer, the robustness of NP voltage and CMV will be compromised since n_1 CVVs of its output are already affected by the parameter mismatch. Therefore, J_i is placed in the last layer to eliminate the coupling degree of robustness.

III. Proposed NNO-Based P3L-SMFPC Method

Fig. 2 shows the control flowchart of the proposed NNO-based P3L-SMFPC method. The main body of this method is a three-layer SMPC. However, the first layer controls the NP voltage without using any cost function. Therefore, the proposed method is regarded as a pseudo-three-layer structure. Moreover, the cost functions of ZSCC and grid-side currents are constructed with discretized ULMs, and NNO is used to observe the uncertain terms.

A. NP Voltage Control

A well-known conclusion about NP voltage control is that a total of 9 CVVs (zero and long vectors) do not affect the NP voltage, while the remaining 18 CVVs (short and medium vectors) do [32]. It can be seen from (6) that if C_1 is a constant, only the expression $|\boldsymbol{u}|^T \boldsymbol{i}_1$ affects the NP voltage. Based on the assumption of a three-phase balance (namely, $i_{1a}+i_{1b}+i_{1c}=0$), the values of $|\boldsymbol{u}|^{\mathrm{T}} \boldsymbol{i}_1$ under all 27 CVVs can be divided into seven groups, as given in Table I. It can be seen from Table I that, except for 0, the value of $|\boldsymbol{u}|^T \boldsymbol{i}_1$ is the value or the opposite of the grid-side current.

TABLE I
CVVs Groups of $|\boldsymbol{u}|^T \boldsymbol{i}_1$

CVVs	$\lvert\boldsymbol{u}\rvert^{\mathrm{T}}\boldsymbol{i}_1$	Group
000, 11-1, 1-11, 1-1-1, -111, -11-1, -1-11, 111, -1-1-1	0	g1
100, -100	i_{1a}	g2
010, 0-10	i_{1b}	g3
001, 00-1	i_{1c}	g4
011, 01-1, 0-11, 0-1-1	$-i_{1a}$	g5
101, 10-1, -101, -10-1	$-i_{1b}$	g6
110, 1-10, -110, -1-10	$-i_{1c}$	g7

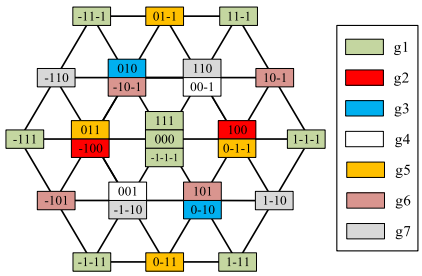

Fig. 3. CVV groups of $|\boldsymbol{u}|^{\mathrm{T}} \boldsymbol{i}_1$ in the space vector diagram of 3LT²C.

TABLE II
CVV Groups Selected Based on the Sampled Values

i_{1a}	i_{1b}	i_{1c}	$u_{np}>0$	$u_{np}<0$
+	-	+	U_1: g1 g3 g5 g7	U_4: g1 g2 g4 g6
+	-	-	U_2: g1 g3 g4 g5	U_5: g1 g2 g6 g7
+	+	-	U_3: g1 g4 g5 g6	U_6: g1 g2 g3 g7
-	+	-	U_4: g1 g2 g4 g6	U_1: g1 g3 g5 g7
-	+	+	U_5: g1 g2 g6 g7	U_2: g1 g3 g4 g5
-	-	+	U_6: g1 g2 g3 g7	U_3: g1 g4 g5 g6
+	+	+	U_7: g1 g2 g3 g4 g5 g6 g7	U_7: g1 g2 g3 g4 g5 g6 g7
-	-	-	U_7: g1 g2 g3 g4 g5 g6 g7	U_7: g1 g2 g3 g4 g5 g6 g7

The CVV groups of $|\boldsymbol{u}|^T \boldsymbol{i}_1$ classified in the space vector diagram of 3LT²C are shown in Fig. 3. Fig. 3 shows that g1 contains all zero and long vectors; $g2$, $g3$, and $g4$ each contains two symmetric short vectors; $g5$, $g6$, and $g7$ each contains two symmetric medium and short vectors.

Suppose that $u_{np}(k)>0$, $|\boldsymbol{u}(k)|^T \boldsymbol{i}_1(k)$ should be less than 0 to ensure $u_{\text{np}}(k+1)<u_{\text{np}}(k)$ according to (7). Also, suppose that $i_{1a}(k)>0$, $i_{1b}(k)<0$, and $i_{1c}(k)>0$. Then the CVVs corresponding to $g3$, $g5$, and $g7$ can be chosen to ensure $|\boldsymbol{u}(k)|^T \boldsymbol{i}_1(k)<0$ so that $u_{\text{np}}(k+1)<u_{\text{np}}(k)$. In addition, g1 should be added to the selection since CVVs in $g1$ have no control effect on u_{np} and are vital to building the outer hexagon structure in Fig. 3. When these CVVs are used as FCS for the cost function, the NP voltage is necessarily suppressed or unchanged no matter which CVV is eventually applied to the system. Therefore, the NP voltage can be effectively suppressed by judging the positive or negative of the sampled values of u_{np} and $\boldsymbol{i}_1$ at each sampling time. Table II gives the proposed NP voltage control method based on the above discussion. Although sixteen cases are enumerated in Table II, only seven combinations of selected CVV groups count, named $U_1,\ldots,$ and U_7. The cost function of ZSCC will select a specific set from U_1 to U_7 as the FCS at each sampling time. According to the analysis of (12), the parameter mismatch does not affect the proposed NP voltage

control method. In addition, this method does not need to obtain the value of dc-bus capacitances, C_1 and C_2.

Remark 3: If the three-phase voltage is balanced, the proposed method can theoretically eliminate the possibility of the continuous increase/decrease of NP voltage. However, due to the existence of ZSCC, the expression of $|\boldsymbol{u}|^T \boldsymbol{i}_1$ is not rigorous. According to (8), the values of $|\boldsymbol{u}|^T \boldsymbol{i}_1$ in the four groups, $g1$, $g5$, $g6$, and $g7$, in Table I, are accurate by adding i_z. In this case, the proposed NP control method will become highly complex and is not conducive to subsequent control. Therefore, the CVV selection method of Table II is still adopted. In addition, ZSCC can cause the values of the three-phase grid-side currents to be totally positive or negative. Table II considers these situations and chooses U_7 as the set of all 27 CVVs to suppress ZSCC sufficiently. The proposed method can still exhibit excellent NP voltage suppression demonstrated by simulation and experiment comparisons and has strong robustness.

B. Ultralocal Model

ULM is a simplified model that describes the nonlinear system, which generally contains one or several uncertain terms to be estimated. According to (3), the ULM of grid-side currents can be expressed as

$$\frac{d\boldsymbol{i}_{1\alpha\beta}}{dt} = \boldsymbol{F} + \gamma \boldsymbol{C}_{3s/2s}\boldsymbol{u} \tag{13}$$

where $\boldsymbol{F} = -\frac{R_1}{L_1}\boldsymbol{i}_{1\alpha\beta} - \frac{1}{L_1}\boldsymbol{v}_{g\alpha\beta}$, and $\gamma = \frac{V_{\rm dc}}{2L_1}$.

In addition, the robustness of ZSCC cannot be achieved by controlling CMV; therefore, the mathematical model of i_z needs to be reconstructed. By combining the three equations in (3) for the grid-side currents, ZSCC can be represented as follows:

$$\frac{di_z}{dt} = -\frac{R_1}{L_1}i_z - \frac{1}{L_1}\begin{bmatrix}1 & 1 & 1\end{bmatrix}\boldsymbol{v}_g + \frac{V_{\rm dc}}{2L_1}\begin{bmatrix}1 & 1 & 1\end{bmatrix}\boldsymbol{u}. \tag{14}$$

Notably, the mathematical model of ZSCC can be built in (9), whose filter parameters are centralized rather than independent; (14) is based on the independent control of each converter and is more suitable for building the ULM.

According to (14), the ULM of ZSCC can be expressed as follows:

$$\frac{di_z}{dt} = f + \gamma\begin{bmatrix}1 & 1 & 1\end{bmatrix}\boldsymbol{u} \tag{15}$$

where $f = -\frac{R_1}{L_1}i_z - \frac{1}{L_1}[1\ 1\ 1]\boldsymbol{v}_g$.

Using the forward Euler formula, the discretized prediction models for $\boldsymbol{i}_1$ and i_z were derived as follows:

$$\boldsymbol{i}_{1\alpha\beta}(k+1) = T_s\left(\boldsymbol{F}^{\rm obs}(k) + \gamma\boldsymbol{C}_{3s/2s}\boldsymbol{u}(k)\right) + \boldsymbol{i}_{1\alpha\beta}(k) \tag{16}$$

$$i_z(k+1) = T_s\left(f^{\rm obs}(k) + \gamma[1\quad 1\quad 1]\boldsymbol{u}(k)\right) + i_z(k) \tag{17}$$

where obs denotes the observed value.

The uncertain terms in the ULMs, expressed in (13) and (15), are $\boldsymbol{F}$ and f, respectively, whereas the certain term γ needs to be predetermined. Although γ contains L_1, the correct estimation of $\boldsymbol{F}$ and f will remove the α bias in the case of parameter mismatch. The detailed proof can be seen in [18] and [19].

C. Design of NNO Observer

The uncertain terms $\boldsymbol{F}$ and f can be estimated by NNO as follows [21]:

$$\begin{cases}\boldsymbol{F} = \boldsymbol{W}^{\rm T}\phi(\boldsymbol{i}_{1\alpha\beta})\\ f = w\phi(i_z)\end{cases} \tag{18}$$

where $\boldsymbol{W}$ and w are the output weights, and $\phi\,(x) = \frac{1}{1+e^{-x}}$ is the activation function.

In (18), the observers of the state variables $\boldsymbol{i}_1$ and i_z are designed as follows:

$$\begin{cases}\frac{d\boldsymbol{i}^{\rm obs}_{1\alpha\beta}}{dt} = (\boldsymbol{W}^{\rm obs})^T\phi(\boldsymbol{i}_{1\alpha\beta}) + \gamma\boldsymbol{C}_{3s/2s}\boldsymbol{u} - k_1(\boldsymbol{i}^{\rm obs}_{1\alpha\beta} - \boldsymbol{i}_{1\alpha\beta})\\ \frac{di^{\rm obs}_z}{dt} = w^{\rm obs}\phi(i_z) + \gamma\begin{bmatrix}1 & 1 & 1\end{bmatrix}\boldsymbol{u} - k_2(i^{\rm obs}_z - i_z)\end{cases} \tag{19}$$

where k_1 and k_2 are set as positive constants.

In addition, the updated laws of the output weights $\boldsymbol{W}$ and w are expressed as follows:

$$\begin{cases}\frac{d\boldsymbol{W}^{\rm obs}}{dt} = -\tau_1\left[\phi(\boldsymbol{i}_{1\alpha\beta})\left(\boldsymbol{i}^{\rm obs}_{1\alpha\beta} - \boldsymbol{i}_{1\alpha\beta}\right)^T + k_{w1}\boldsymbol{W}^{\rm obs}\right]\\ \frac{dw^{\rm obs}}{dt} = -\tau_2\left[\phi(i_z)\left(i^{\rm obs}_z - i_z\right) + k_{w2}w^{\rm obs}\right]\end{cases} \tag{20}$$

where τ_1, τ_2, k_{w1}, and k_{w2} are set as positive constants.

Then, the discretized estimation of the uncertain terms $\boldsymbol{F}$ and f using the backward Euler method can be derived as follows:

$$\begin{cases}\boldsymbol{i}^{\rm obs}_{1\alpha\beta}(k) = \boldsymbol{i}^{\rm obs}_{1\alpha\beta}(k-1) + T_s[\boldsymbol{W}^{\rm obs}(k-1)]^T\phi[\boldsymbol{i}_{1\alpha\beta}(k-1)]\\ +T_s\gamma\boldsymbol{C}_{3s/2s}\boldsymbol{u}(k-1) - T_sk_1[\boldsymbol{i}^{\rm obs}_{1\alpha\beta}(k-1) - \boldsymbol{i}_{1\alpha\beta}(k-1)]\\ \boldsymbol{W}^{\rm obs}(k) = (1 - T_s\tau_1k_{w1})\boldsymbol{W}^{\rm obs}(k-1)\\ -T_s\tau_1\phi[\boldsymbol{i}_{1\alpha\beta}(k-1)][\boldsymbol{i}^{\rm obs}_{1\alpha\beta}(k-1) - \boldsymbol{i}_{1\alpha\beta}(k-1)]^T\\ \boldsymbol{F}^{\rm obs}(k) = [\boldsymbol{W}^{\rm obs}(k)]^{\rm T}\phi[\boldsymbol{i}_{1\alpha\beta}(k)]\end{cases} \tag{21}$$

$$\begin{cases}i^{\rm obs}_z(k) = i^{\rm obs}_z(k-1) + T_sw^{\rm obs}(k-1)\phi[i_z(k-1)]\\ \quad +T_s\gamma\,[111]\,\boldsymbol{u}(k-1) - T_sk_2[i^{\rm obs}_z(k-1) - i_z(k-1)]\\ w^{\rm obs}(k) = (1 - T_s\tau_2k_{w2})w^{\rm obs}(k-1)\\ \quad -T_s\tau_2\phi[i_z(k-1)][i^{\rm obs}_z(k-1) - i_z(k-1)]\\ f^{\rm obs}(k) = w^{\rm obs}(k)\phi[i_z(k)]\end{cases} \tag{22}$$

It should be noted that the iterative algorithm for NNO in (21) and (22) requires assigning initial values to all observed values. The initial values of the output weights $\boldsymbol{W}^{\rm obs}$ and $w^{\rm obs}$ were set to $\boldsymbol{I}_{2*2}$ and 1, respectively, and the others were set to zeros or zero vectors.

Fig. 4 shows the structure of the proposed NNO, using (21) as an example. As shown in Fig. 4, NNO can be divided into three parts. First, the state variables $\boldsymbol{i}_1$ are observed. Secondly, the weight of the neural network, $\boldsymbol{W}$, is updated by the observed values of state variables. Finally, the updated input-output relationship is obtained by the activation function and the updated weight, and the observed value of the uncertain term $\boldsymbol{F}$ can be obtained.

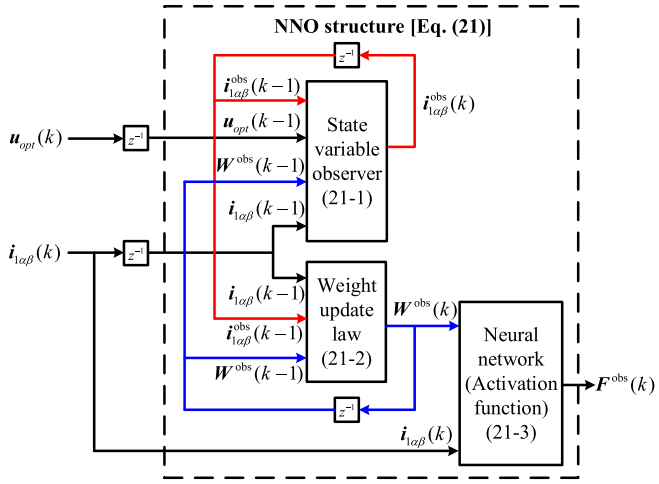

Fig. 4. Proposed NNO structure.

TABLE III
CVV GROUPS OF U_7

CVVs	Selected CVV	Group
111	111	U_7^1
011, 101,110	011	U_7^2
001, 010, 100,11-1, 1-11, -111	001	U_7^3
000, 01-1, 0-11, 10-1, -101, 1-10, -110	000	U_7^4
00-1, 0-10, -100, 1-1-1, -11-1, -1-11	00-1	U_7^5
0-1-1, -10-1, -1-10	0-1-1	U_7^6
-1-1-1	-1-1-1	U_7^7

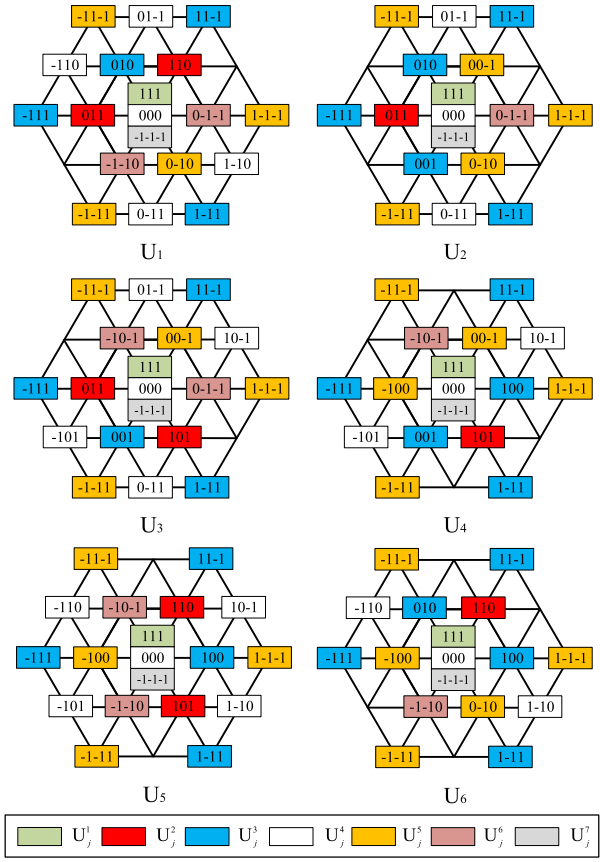

Fig. 5. CVV groups of U_1 to U_6 in the space vector diagram of 3LT^{2}C.

D. Pseudo-Three-Layer SMPC

According to the discretized ULM, expressed in (16) and (17), the cost functions of $\boldsymbol{i}_1$ and i_z were designed as follows:

$$J_i^{\text{ULM}} = \left\| T_s(\boldsymbol{F}^{\text{obs}}(k) + \gamma \boldsymbol{C}_{3s/2s}\boldsymbol{u}(k)) + \boldsymbol{i}_{1\alpha\beta}(k) - \boldsymbol{i}_{1ref}(k+1) \right\| \quad (23)$$

$$J_z^{\text{ULM}} = \left| T_s(f^{\text{obs}}(k) + \gamma [\,1 \quad 1 \quad 1\,]\boldsymbol{u}(k)) + i_z(k) \right|. \quad (24)$$

In the control flowchart (see Fig. 2), J_z^{ULM} is located in the second and J_i^{ULM} in the third layers. As mentioned, the proposed NP voltage control enables J_z^{ULM} to obtain seven different FCSs, namely $U_1, \ldots,$ and U_7. Suppose that at some time, the FCS obtained by J_z^{ULM} is U_7, which is the set formed by all 27 CVVs. According to the expression in (24), due to the existence of vector $[1\ 1\ 1]$, when $\boldsymbol{u}(k)$ is $[1\ 0\ 0]^T$ or $[0\ 1\ 0]^T$ or $[0\ 0\ 1]^T$, the corresponding values of J_z^{ULM} are the same. In other words, the above three CVVs have the same control effect. Followed by this idea, all 27 CVVs can be divided into seven groups, named $U_7^1, \ldots,$ and U_7^7, as given in Table III. When the FCS is U_7, J_z^{ULM} only needs to be calculated exhaustively 7 times instead of 27 times.

Suppose that at some time, the FCS obtained by J_z^{ULM} is one of U_1 to U_6, which is the set formed by less than 27 CVVs. Interestingly, any U_1 to U_6 can still be divided into seven groups based on the control effect. Fig. 5 shows the CVV groups of U_1 to U_6 classified in the space vector diagram of 3LT^{2}C. Even though U_j $(j = 1, \ldots, 6)$ is a subset of U_7, U_j can still be divided into 7 groups, denoted as $U_j^1, \ldots,$ and U_j^7. To summarize, the following relationship can be obtained as

$$\forall i = 1, \ldots, 7 \forall j = 1, \ldots, 6, U_j^i \subset U_7^i. \quad (25)$$

Therefore, whichever FCS of J_z^{ULM} is from U_1 to U_7, it only needs the seven selected CVVs in Table III, defined as the simplified FCS, for J_z^{ULM} to calculate. The computational burden can be significantly reduced.

An example of the execution flow of the proposed P3L-SMPC method is shown in Fig. 6. In the first layer, U_j is selected in Table II according to the sampling information. In the second layer, m suboptimal solutions (including an optimal solution) are computed by substituting the simplified FCS (the seven CVVs in Table III) into J_z^{ULM}. Since the simplified FCS only applies to J_z^{ULM} rather than J_i^{ULM}, the m CVVs must be restored to the n_2 CVVs required for J_i^{ULM}, defined as the reconstructed FCS, according to Table III or Fig. 5. In layer III, the reconstructed FCS is substituted into J_i^{ULM}, and the optimal solution of the proposed structure is obtained. It is worth noting that the proposed P3L-SMPC only needs to design one parameter: the weighting number m.

Remark 4: The proposed method is called a pseudo-three-layer structure because the first layer has no cost function, and the CVVs of the second layer (namely the simplified FCS) are time-invariant and design-free. Therefore, only one weighting

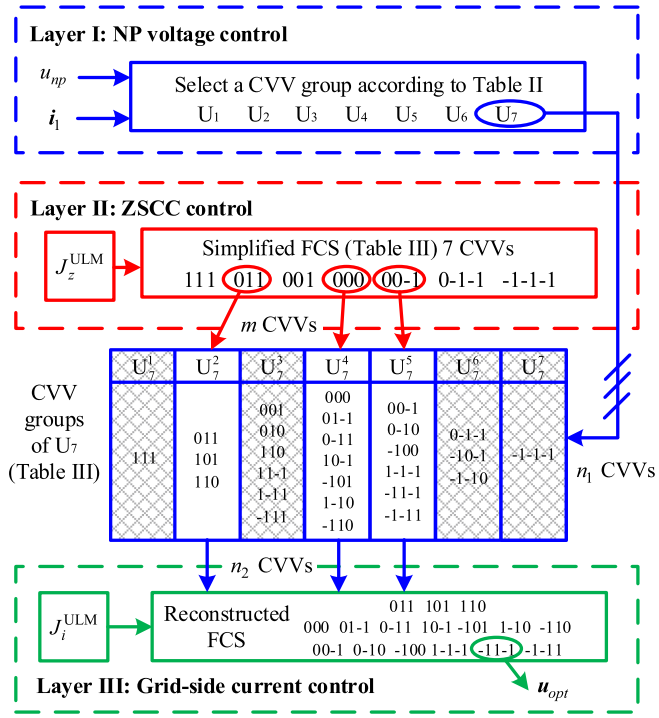

Fig. 6. Implementation example of the proposed P3L-SMPC method.

number m is designed for the pseudo-three-layer structure. On the contrary, the three-layer structure can be seen in (12), where there are two weighting, factors to design, which becomes more time-consuming.

E. Stability Analysis

In this section, the estimation error system is established and its input-to-state stability (ISS) is proved by Lyapunov-based analysis. First, the estimation errors of $\boldsymbol{W}$, w, $\boldsymbol{i}_{1\alpha\beta}$, and $i_z$are defined as follows:

$$\begin{cases} \widetilde{\boldsymbol{W}} = \boldsymbol{W}^{\text{obs}} - \boldsymbol{W} \\ \widetilde{w} = w^{\text{obs}} - w \\ \widetilde{\boldsymbol{i}_{1\alpha\beta}} = \boldsymbol{i}_{1\alpha\beta}^{\text{obs}} - \boldsymbol{i}_{1\alpha\beta} \\ \widetilde{i_z} = i_z^{\text{obs}} - i_z \end{cases}. \tag{26}$$

According to the ULMs [(13) and (15)] and the observation models [(19) and (20)], the state space equation for the estimation error can be easily derived as follows:

$$\begin{cases} \frac{d\widetilde{\boldsymbol{W}}}{dt} = -\tau_1 \left[\phi\left(\boldsymbol{i}_{1\alpha\beta}\right) \left(\widetilde{\boldsymbol{i}_{1\alpha\beta}}\right)^{\mathrm{T}} + k_{w1} \boldsymbol{W}^{\text{obs}} \right] \\ \frac{d\widetilde{w}}{dt} = -\tau_2 \left[\phi(i_z) \left(\widetilde{i_z}\right)^{\mathrm{T}} + k_{w2} w^{\text{obs}} \right] \\ \frac{d\widetilde{\boldsymbol{i}_{1\alpha\beta}}}{dt} = \left(\widetilde{\boldsymbol{W}}\right)^{\mathrm{T}} \phi(\boldsymbol{i}_{1\alpha\beta}) - k_1 \widetilde{\boldsymbol{i}_{1\alpha\beta}} \\ \frac{d\widetilde{i_z}}{dt} = (\widetilde{w})^{\mathrm{T}} \phi(i_z) - k_2 \widetilde{i_z} \end{cases}. \tag{27}$$

Consider the following Lyapunov function:

$$V = \frac{1}{2}\left(\widetilde{\boldsymbol{i}_{1\alpha\beta}}\right)^T \widetilde{\boldsymbol{i}_{1\alpha\beta}} + \frac{1}{2}\left(\widetilde{i_z}\right)^T \widetilde{i_z} + \frac{1}{2\tau_1} \text{tr}\left[\left(\widetilde{\boldsymbol{W}}\right)^{\mathrm{T}} \widetilde{\boldsymbol{W}}\right] + \frac{1}{2\tau_2} \text{tr}\left[(\widetilde{w})^T \widetilde{w}\right]. \tag{28}$$

The derivative of (28) yields

$$\begin{aligned} \dot{V} = & \left(\widetilde{\boldsymbol{i}_{1\alpha\beta}}\right)^T \dot{\widetilde{\boldsymbol{i}_{1\alpha\beta}}} + \left(\widetilde{i_z}\right)^T \dot{\widetilde{i}}_z + \frac{1}{\tau_1} \text{tr}\left[\left(\widetilde{\boldsymbol{W}}\right)^T \dot{\widetilde{\boldsymbol{W}}}\right] \\ & + \frac{1}{\tau_2} \text{tr}\left[(\widetilde{w})^T \dot{\widetilde{w}}\right] \\ = & \left(\widetilde{\boldsymbol{i}_{1\alpha\beta}}\right)^T \left(\widetilde{\boldsymbol{W}}\right)^T \phi\left(\boldsymbol{i}_{1\alpha\beta}\right) - k_1 \left(\widetilde{\boldsymbol{i}_{1\alpha\beta}}\right)^T \widetilde{\boldsymbol{i}_{1\alpha\beta}} \\ & + \left(\widetilde{i_z}\right)^T (\widetilde{w})^T \phi(i_z) - k_2 \left(\widetilde{i_z}\right)^{\mathrm{T}} \widetilde{i_z} \\ & - \text{tr}\left[\left(\widetilde{\boldsymbol{W}}\right)^T \phi\left(\boldsymbol{i}_{1\alpha\beta}\right) \left(\widetilde{\boldsymbol{i}_{1\alpha\beta}}\right)^T\right] - k_{w1} \text{tr}\left[\left(\widetilde{\boldsymbol{W}}\right)^{\mathrm{T}} \boldsymbol{W}^{\text{obs}}\right] \\ & - \text{tr}\left[(\widetilde{w})^T \phi\left(\boldsymbol{i}_{1\alpha\beta}\right) \left(\widetilde{\boldsymbol{i}_{1\alpha\beta}}\right)^T\right] - k_{w2} \text{tr}\left[(\widetilde{w})^{\mathrm{T}} w^{\text{obs}}\right] \\ = & -k_1 \left(\widetilde{\boldsymbol{i}_{1\alpha\beta}}\right)^T \widetilde{\boldsymbol{i}_{1\alpha\beta}} - k_{w1} \text{tr}\left[\left(\widetilde{\boldsymbol{W}}\right)^T \widetilde{\boldsymbol{W}}\right] \\ & - k_{w1} \text{tr}\left[\left(\widetilde{\boldsymbol{W}}\right)^T \boldsymbol{W}\right] \\ & - k_2 \left(\widetilde{i_z}\right)^T \widetilde{i_z} - k_{w2} \text{tr}\left[(\widetilde{w})^T \widetilde{w}\right] - k_{w2} \text{tr}\left[(\widetilde{w})^T w\right] \\ \le & -k_1 \left\|\widetilde{\boldsymbol{i}_{1\alpha\beta}}\right\|^2 - k_{w1} \left\|\widetilde{\boldsymbol{W}}\right\|_F^2 + k_{w1} \left\|\widetilde{\boldsymbol{W}}\right\|_F \|\boldsymbol{W}\|_F \\ & - k_2 \left\|\widetilde{i_z}\right\|^2 - k_{w2} \|\widetilde{w}\|_F^2 + k_{w1} \|\widetilde{w}\|_F \|w\|_F. \end{aligned} \tag{29}$$

To simplify (29), define the following variables:

$$\begin{cases} \boldsymbol{\varepsilon} = \left[\left\|\widetilde{\boldsymbol{i}_{1\alpha\beta}}\right\|, \left\|\widetilde{i_z}\right\|, \left\|\widetilde{\boldsymbol{W}}\right\|_F, \|\widetilde{w}\|_F\right]^T \\ \kappa = \min(k_{w1}, k_{w2}) \\ \boldsymbol{\xi} = \left[\kappa \|\boldsymbol{W}\|_F, \kappa \|w\|_{\mathrm{F}}\right]^T \\ h = \min(k_1, k_2, k_{w1}, k_{w2}) \end{cases}. \tag{30}$$

Therefore, (29) can be rewritten as

$$\dot{V} \le -h\|\boldsymbol{\varepsilon}\|^2 + \|\boldsymbol{\xi}\| \|\boldsymbol{\varepsilon}\|. \tag{31}$$

If and only if the following is satisfied:

$$h\delta \|\boldsymbol{\varepsilon}\| \ge \|\boldsymbol{\xi}\| \tag{32}$$

where $0 < \delta < 1$, one has

$$\dot{V} \le -h(1-\delta)\|\boldsymbol{\varepsilon}\|^2 < 0. \tag{33}$$

Thus, it can be obtained that the estimation error system (27) is ISS, and the estimation errors are uniformly ultimately bounded. It should be noted that δ is a fictitious parameter, which can only prove that the derivative of the Lyapunov function is less than zero in a specific range, and cannot be used to adjust the controller. The parameters that can adjust the controller are k_1, k_2, k_{w1}, k_{w2}, τ_1, and τ_2, shown in (21) and (22). The selection of these parameters is explained in the following section.

TABLE IV
SIMULATION PARAMETERS

Parameter	Description	Values
V_{dc} (V)	DC-bus voltage	300
C_1, C_2 (μF)	DC-bus capacitance	500
L_1 (mH)	Nominal value of filter inductance	10
R_1 (Ω)	Parasitic resistance	0.02
V_g (V)	Grid voltage (peak value)	100
$I^{(1)}_{2ref\alpha\beta}$ (A)	Current reference amplitude of 3LT^{2}C-1	15
$I^{(1)}_{2ref\alpha\beta}$ (A)	Current reference amplitude of 3LT^{2}C-2	25
ω (rad/s)	Grid frequency	314.16
m	weighting number	3

IV. SIMULATION VERIFICATIONS

A. Parameter Selection

In this section, the superiority of the proposed method is demonstrated by simulation results. The NP voltage oscillations, total grid-side currents, and ZSCC features draws the most attention. The parameters of the parallel 3LT^{2}C system are given in Table IV. It should be noted that the suppression effect of ZSCC can be easily observed from the two 3LT^{2}Cs adjusted to different current reference amplitudes given in Table IV.

The NNO in (21) and (22) show two neural network structures, with each NNO containing two input nodes and one output node. The NNO in this article only stores the information at sampling time k-1, which means that each NNO has only one hidden layer. Nevertheless, NNO is capable of observing uncertain terms accurately. Second, the predictor gains k_1 and k_2 are mainly responsible for system stability. Too high value of k_1 and k_2 may incur system oscillation. Besides, k_{w1} and k_{w2} are used to adjust the adaptability of NNO to parameter mismatch. If k_{w1} and k_{w2} are too large, adaptability will be inhibited. Finally, τ_1 and τ_2 are chosen to ensure system stability and to increase the tracking performance. Although there are multiple parameters that need to be adjusted by trial-and-error, in this scenario, the selection ranges of these parameters are very wide. In simulation tests, parameter changes of up to five orders of magnitude do not affect the control effect. In [21] and [22], the following control parameters were established for the NNO: $k_1 = k_2 = 10\,000$; $k_{w1} = k_{w2} = 0.01$; and $\tau_1 = \tau_2 = 100$.

Moreover, for P3L-SMFPC method, according to Fig. 6, the P3L-SMFPC only needs to design a CVVs number m, whose selection range is an integer ranging from 2 to 6. The larger m is, the better the control effect on the grid-side current is, and the worse the suppression effect on ZSCC is. In this article, m is set to 3.

The following FCS-MPC-based methods are selected for comparison with the proposed method in simulation and experiments.

1) *Conventional FCS-MPC:* Its cost function is shown in (11), where $\lambda_{\text{np}} = 0.2$ and $\lambda_{cmv} = 0.1$.
2) *ESO-Based MFPC:* J_i^{ULM} and J_z^{ULM} expressed in (23) and (24), were used for obtaining robust control of grid-side current and ZSCC, respectively. The uncertain terms were estimated by the ESO [18], [19]. The cost function of this method is given as

$$J(k) = J_i^{\text{ULM}}(k) + \lambda_{\text{np}} J_{\text{np}}(k) + \lambda_z J_z^{\text{ULM}}(k) \tag{34}$$

where $\lambda_{\text{np}} = 0.1$ and $\lambda_z = 0.4$.
3) *ESO-Based SMFPC:* The simplified SMPC method in [31] was established, where J_i was replaced by the robust J_i^{ULM}, whose uncertain term was estimated by the ESO. The CVV was set to 5.
4) *ESO-Based VV-MFPC:* The method proposed in [24] was adopted for comparison. In addition to using ESO to observe the uncertainty of current cost function, VVs were utilized to inhibit the ZSCC.
5) *ESO-Based P3L-SMFPC:* The proposed P3L-SMFPC structure is adopted in this method, but the observer is replaced by ESO.

B. Simulation Result Analysis

The performance of the proposed method for a parallel-3LT^{2}C was verified using MATLAB/Simulink. In the simulation, the actual value of $L_1^{(1)}$ was 150%, 100%, and 50% of the nominal value, the actual value of $L_1^{(2)}$ was 150%, and the sample time was set to 50 μs.

1) Simulation Results of Different MFPC Methods: Fig. 7 illustrates the simulation waveforms of the six methods, including the total grid-side currents and their errors, the NP voltages of 3LT^{2}C-1, and the ZSCC. First, the THDs of the six methods can be observed to rose as $L_1^{(1)}$ decreased. However, the waveform distortion of conventional FCS-MPC was the most obvious in Fig. 7(a), while the other three model-free methods all exhibited small THDs and high robustness. The THD of the proposed method (1.38%) is larger than that of ESO-MFPC (1.35%) but smaller than that of ESO-SMFPC (1.55%), ESO-VV-MFPC (2.14%), and ESO-P3L-SMFPC (1.70%). Second, the current tracking error of the proposed method was the smallest, as can be seen from Fig. 7(d), while other ESO-based methods possessed sinusoidal current errors from Fig. 7(b)–(e), indicating that the NNO observed the uncertain terms of ULMs more accurate than ESO. Thirdly, it can be seen from Fig. 7(a) and (b) that the NP voltages of both conventional FCS-MPC and ESO-MFPC decreased with the increase of $L_1^{(1)}$, and the latter was more prominent than the former. This phenomenon is because the weighted cost function makes multiple control objectives become a whole so that the NP voltage that is independent of $L_1^{(1)}$ is still affected by $L_1^{(1)}$. At the same time, the weighting factor design also affects the NP voltage's robustness. In contrast, the NP voltages under the two SMPC-based methods (NNO-SMFPC and proposed method) were not affected by $L_1^{(1)}$, as can be seen from Fig. 7(c) and (d). Finally, compared with the traditional FCS-MPC, all five MFPC methods showed smaller ZSCC, while the ESO-VV-MFPC had the smallest peak-to-peak value of ZSCC, as can be seen from Fig. 7(d). ESO-VV-MFPC used only seven CVVs that make CMV zero, and the VVs were also synthesized from these seven vectors. In this way, the NP voltage becomes the only excitation source of ZSCC, which maximizes the suppression effect of ZSCC. However, the reduction of CVVs

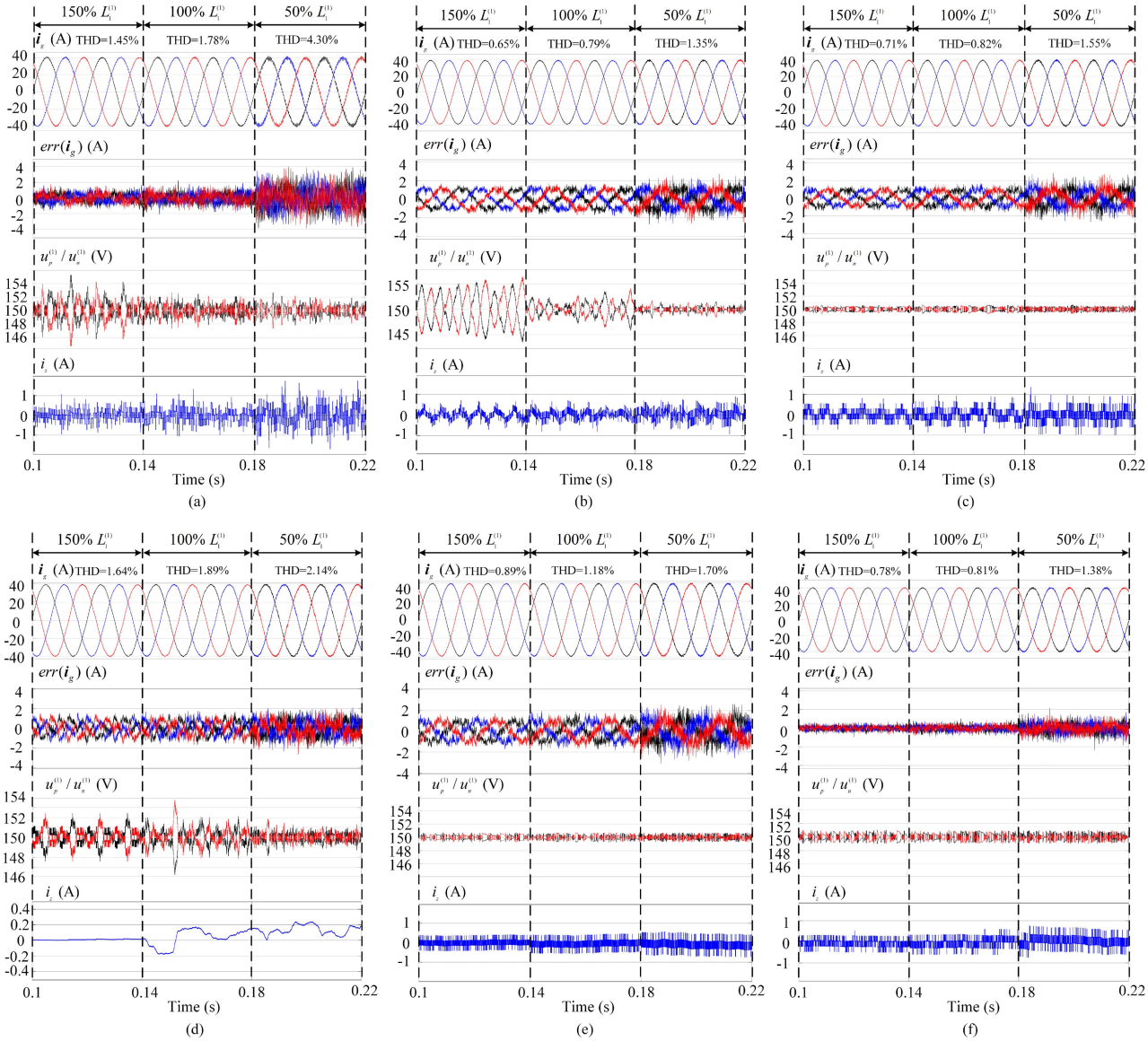

Fig. 7. Simulation results under parameter mismatch. (a) Conventional FCS-MPC. (b) ESO-MFPC. (c) ESO-SMFPC. (d) ESO-VV-MFPC. (e) ESO-P3L-SMFPC. (f) Proposed method.

also means that the control effect of grid-side currents and NP voltage becomes worse. In comparison, the proposed method suppresses ZSCC incompletely, but showed better control effect of currents and NP-voltage, as seen in Fig. 7(f).

2) Simulation Comparison Between MFPC Methods: For quantitative analysis, the average errors of $\boldsymbol{i}_g$, $u_{np}^{(1)}$ and i_z were used as follows:

$$\text{avgerr}(\boldsymbol{i}_g) = \frac{1}{n}\sum_{k=1}^{n}\left|\boldsymbol{i}_g(k) - \boldsymbol{i}_{g\text{ref}}(k)\right| \tag{35}$$

$$\text{avgerr}(u_{\text{np}}^{(1)}) = \frac{1}{n}\sum_{k=1}^{n}\left|u_{\text{np}}^{(1)}(k) - 0\right| \tag{36}$$

$$\text{avgerr}(i_z) = \frac{1}{n}\sum_{k=1}^{n}\left|i_z(k) - 0\right| \tag{37}$$

where n denoted the number of sampling points and was set to 800. The above expressions characterize the ability to track the references.

Fig. 8 illustrates the THDs of $\boldsymbol{i}_g$ and the average errors of $\boldsymbol{i}_g$, $u_{\text{np}}^{(1)}$, and i_z of the five MFPC-based methods. In the simulation, $L_1^{(1)}$ changed from 5 to 15 mH, and $L_1^{(2)}$ was kept at 15 mH. In Fig. 8(a), the currents under the five methods all exhibited tiny distortions. However, the proposed method showed the most excellent current-tracking ability while ensuring output quality, as seen in Fig. 8(b). As for the NP voltage, Fig. 8(c) shows that the average errors of $u_{\text{np}}^{(1)}$ under ESO-SMPFC and the proposed method were minimal and not affected by $L_1^{(1)}$. On the contrary, the average error of the NP voltage under ESO-MFPC was significant and the robustness was poor. Finally, the ESO-VV-MFPC presented the best ZSCC suppression capability, as shown in Fig. 8(d).

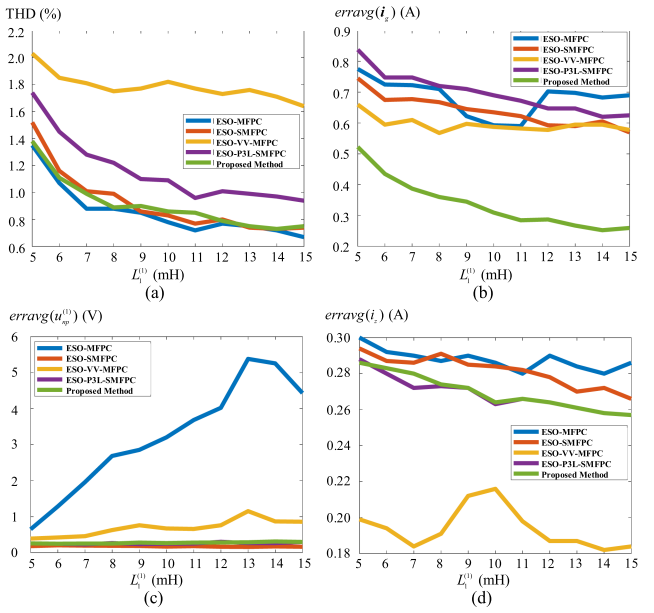

Fig. 8. Simulation comparison of the five MFPC methods under parameter mismatch. (a) THDs of $\boldsymbol{i}_g$. (b) Average errors of $\boldsymbol{i}_g$. (c) Average errors of $u_{\mathrm{np}}^{(1)}$. (d) Average errors of i_z.

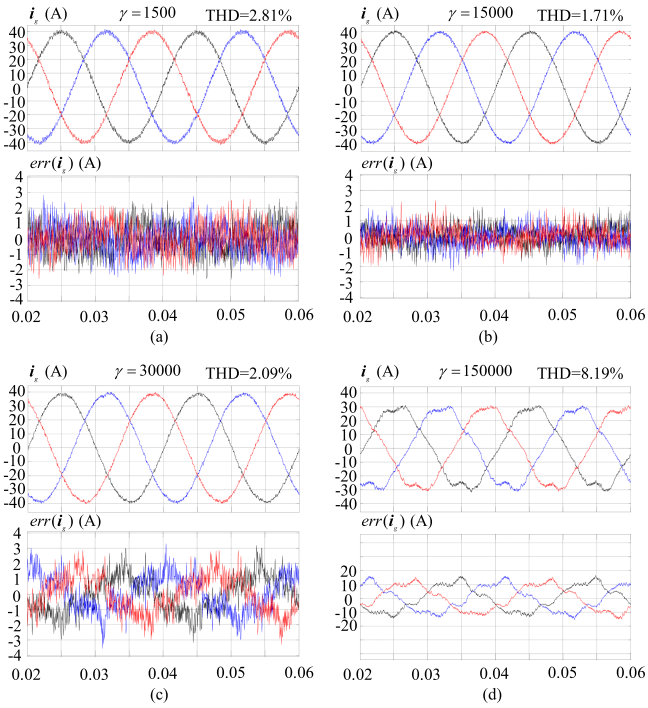

Fig. 9. Simulation results of the total grid-side currents and their errors under the proposed method. (a) $\gamma = 1500$. (b) $\gamma = 15\,000$. (c) $\gamma = 30\,000$. (d) $\gamma = 150\,000$.

3) Influence of Certain Term on the Control Effect: If the nominal value of L_1 is known, the certain term γ in the ULM is preferable to be set to $\frac{V_{\mathrm{dc}}}{2L_1}$. In this article, $V_{\mathrm{dc}} = 300$ V, and $L_1 = 10$ mH, so γ was set to 15 000. However, if nominal value of L_1 is unknown, γ needs to be tuned carefully. If γ is set too large or too small, it will have a significant negative impact on the control effect. Fig. 9 shows the simulation results of total grid-side currents and their errors of the proposed method when $\gamma = 1500, \gamma = 15\,000, \gamma = 30\,000$, and $\gamma = 150\,000$. As can be seen from Fig. 9(a) and (c), when $\gamma = 1500$ or $\gamma = 30\,000$, the grid-side currents can track the reference values, but the THD was relatively large; when $\gamma = 150\,000$, the grid-side currents cannot even track the reference values, as can be seen from Fig. 9(d). In conclusion, if nominal value of L_1 is known, there is no need for online adjustment of the certain term γ, the original value of γ can achieve an ideal control effect.

4) Discussion of Switching Frequency: Although FCS-MPC generally cannot achieve a fixed switching frequency, the average switching frequency can be adopted to compare with different control methods quantitively. The average switching frequency is defined as follows:

$$f_s = 50(N_r + N_f) \tag{38}$$

where N_r and N_f represent the number of rising and falling edges of the switching signals within 20 ms, respectively. The vertical switching device $S_{a1}^{(1)}$ was selected as the test object, and the simulation conditions are the same as those in Fig. 8.

Fig. 10 illustrates the average switching frequencies of the five MFPC-based methods, and $L_1^{(1)}$ changed from 5 to 15 mH. In Fig. 10, the switching frequencies of all five methods tended to decrease as the inductance increased. However, only the ESO-MFPC showed a significant reduction in switching frequency,

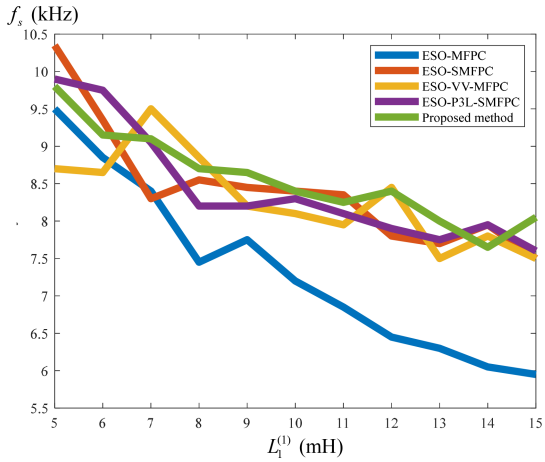

Fig. 10. Switching frequency comparison of the five MFPC methods under parameter mismatch.

and the other four methods (including the proposed method) demonstrated similar switching frequency characteristics. The main reason for this phenomenon is that ESO-MFPC has the worst inhibition effect on NP voltage. As can be seen from Fig. 7(b), the NP voltage corresponding to ESO-MFPC has the worst robustness. In other words, ESO-MFPC does not generate additional switching signals to suppress the NP voltage. However, to ensure the robustness of the NP voltage, the other four methods, including the proposed method, result in the generation of additional switching signals, further increasing the switching frequency. In conclusion, the proposed method sacrifices switching frequency to achieve optimal NP voltage control.

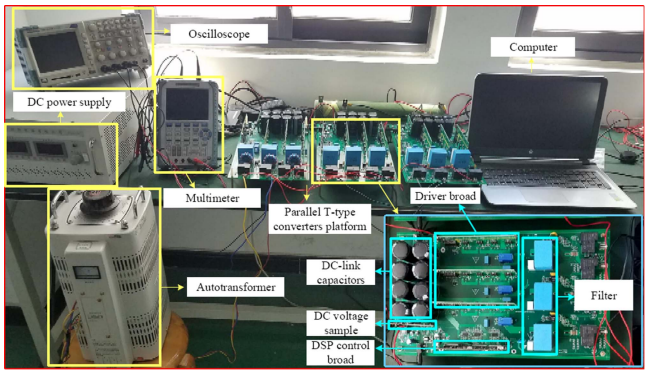

Fig. 11. Experimental Setup.

V. Experiment Results

A. Hardware Setup

The experimental setup is shown in Fig. 11. A 32-bit floating-point digital-signal-processor (DSP), called the TMS320F28379 (Texas Instrument Company, USA), was used for implementation of the control algorithm. This microprocessor is often used for quick and high-speed digital computations. The 3LT^{2}C consists of six FUZI 1MBH50D-060 IGBTs and six FUZI 2MBI150U2A-060 IGBTs. Six Hall current sensors (HCS-LTS-06A) were used to measure the converter current and grid current. A fundamental frequency transformer was applied for voltage matching between the converter and grid voltages. In experiment, the actual value of $L_1^{(1)}$ is 50% of the nominal value, the actual value of $L_1^{(2)}$ is 150% of the nominal value, and the sample time was set to 100 μs. Considering the power level (10-kW) of 3LT^{2}C converter. The reference grid current for 3LT^{2}C-1 and 3LT^{2}C-2 are given to be the same with Table IV.

B. Results and Analysis

1) Experimental Results of Different MFPC Methods Under Parameter Mismatch: Fig. 12 illustrates the experimental waveforms of the six typical methods (conventional FCS-MPC, ESO-MFPC, ESO-SMFPC, ESO-VV-MFPC, ESO-P3L-SMFPC, and proposed method.) with the current reference of $i_{1\alpha}^{\text{ref}} = 15$ A for 3LT^{2}C-1, and $i_{2\alpha}^{\text{ref}} = 25$ A for 3LT^{2}C-2, including the total grid-side currents and their errors under $\alpha\beta$-frame, the NP voltages of 3LT^{2}C-1 and 3LT^{2}C-2, and the ZSCC. Fig. 12(a) shows that under parameter mismatch, the conventional FCS-MPC exhibited significant current distortion (THD = 7.94%) and tracking error, the NP voltage was not effectively suppressed, and the ZSCC oscillation was considerable. In contrast with Fig. 12(a), in Fig. 12(b) and (c), ESO-MFPC and ESO-SMFPC remarkably diminished the current distortion (THD = 3.72% and 4.26%, respectively), but there were still non-negligible tracking errors. ESO-MFPC presented an insufficient NP voltage suppression effect, while ESO-SMFPC had the opposite effect. In addition, both methods demonstrated decent suppression capability in terms of ZSCC. In addition, it can be seen from Fig. 12(d) that ESO-VV-MFPC exhibits the best ZSCC inhibition and good NP voltage balance, but relatively large current distortion

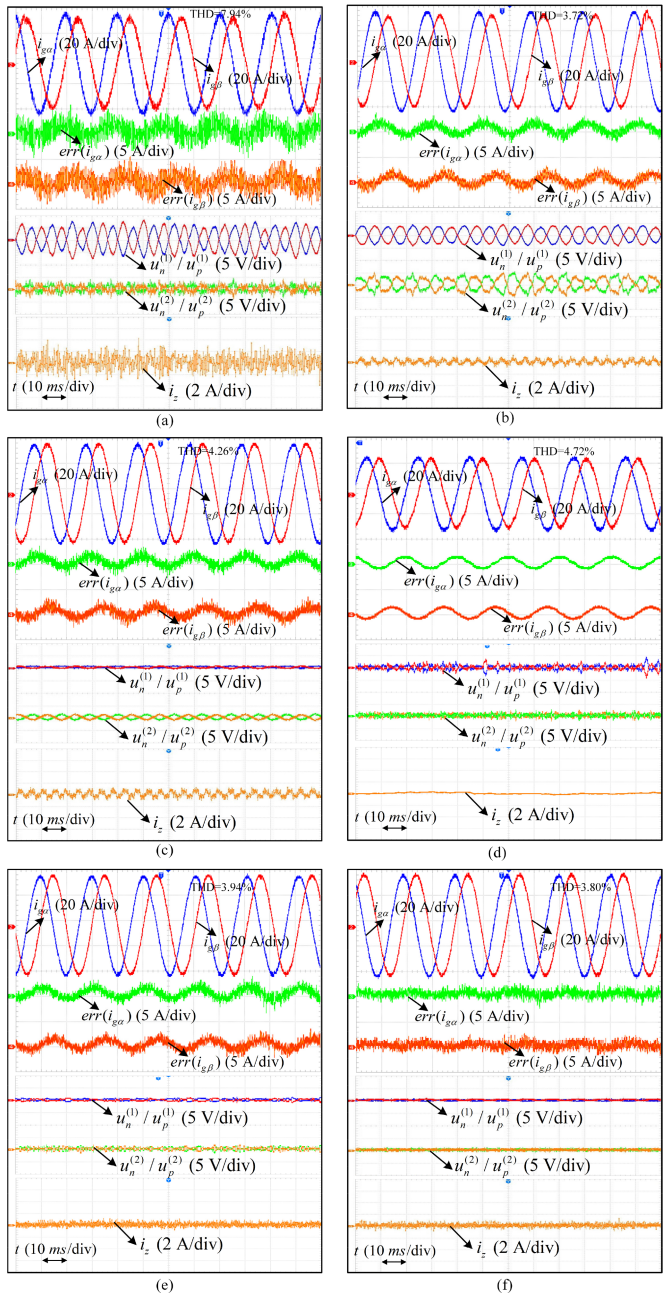

Fig. 12. Experiment results under $\alpha\beta$-frame considering parameter mismatch. (a) Conventional FCS-MPC. (b) ESO-MFPC. (c) ESO-SMFPC. (d) ESO-VV-MFPC. (e) ESO-P3L-SMFPC. (f) Proposed method.

(THD = 4.72%). The results of ESO-based P3L-SMFPC and the proposed method are shown in Fig. 12(e) and (f). In addition to the significant difference in the tracking ability of reference values [THD = 3.94% for Fig. 12(e) and THD = 3.80% for Fig. 12(f)], the two methods showed the best NP voltage balance and excellent ZSCC suppression effect. The above experimental results validate the superiority of the proposed method.

2) Experimental Comparison Between MFPC Methods: Fig. 13 illustrates the THDs of $\boldsymbol{i}_g$ and the average errors of $\boldsymbol{i}_g$, $u_{\text{np}}^{(1)}$, and i_z of the five MFPC-based methods. In the experiment, $L_1^{(1)}$ changed from 5 to 15 mH, and $L_1^{(2)}$ was kept at 15 mH. In

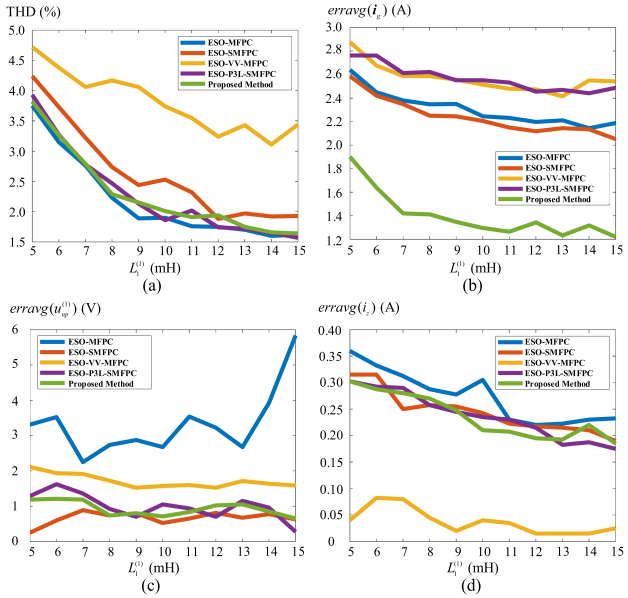

Fig. 13. Experiment comparison of the five MFPC methods under parameter mismatch. (a) THDs of $\boldsymbol{i}_g$. (b) Average errors of $\boldsymbol{i}_g$. (c) Average errors of $u_{\mathrm{np}}^{(1)}$. (d) Average errors of i_z.

Fig. 13(a), with the exception of ESO-VV-MFPC, the remaining methods maintain a small current distortion. However, as shown in Fig. 13(b), the proposed technique demonstrated the best current-tracking capabilities while maintaining output quality. As for the NP voltage, Fig. 13(c) shows that the average errors of $u_{\mathrm{np}}^{(1)}$ under the proposed method was minimal and not affected by $L_1^{(1)}$. On the contrary, for ESO-MFPC, a significant rise in the average error of NP voltage was observed when the inductance value rose. Finally, the ESO-VV-MFPC presented the best ZSCC suppression capability, as shown in Fig. 13(d). In general, the proposed method exhibits excellent multiobjective control effect and robustness, except that the suppression of ZSCC is inferior to that of ESO-VV-MFPC.

3) Dynamic Responses: Fig. 14 displays the dynamic experiment with five different methods. The inductance values were not mismatched during the dynamic test, and the reference value of the total grid-side current increased from 25 to 50 A. Five methods are compared, the results show that, THDs before and after the current reference changes are: THD = 6.85% and 4.57% for conventional FCS-MPC [see Fig. 14(a)], THD = 2.00% and 1.76% for ESO-MFPC [see Fig. 14(b)], THD = 2.84% and 2.70% for ESO-SMFPC [see Fig. 14(c)], THD = 3.63% and 4.06% for ESO-SMFPC [see Fig. 14(d)]. As displayed in Fig. 14(e), the ESO-SMFPC demonstrated quick current dynamic response and good current quality (THD = 2.57% and 2.50%), but current imbalance was noticed. The proposed approach, in contrast, demonstrated quick current dynamic response and good current quality analogously (THD = 2.77% and 2.61%), the NP voltage and ZSCC showed only little increases without spikes, indicating a smoother dynamic performance, as shown in Fig. 14(f).

4) Power Factor of the System: To validate the efficiency of the proposed method, the waveforms of the grid voltage and grid current for phase-A are given and shown in Fig. 15. The results show that the grid voltage is almost in phase with the grid current, indicating a very high power factor (about 0.98) of the system.

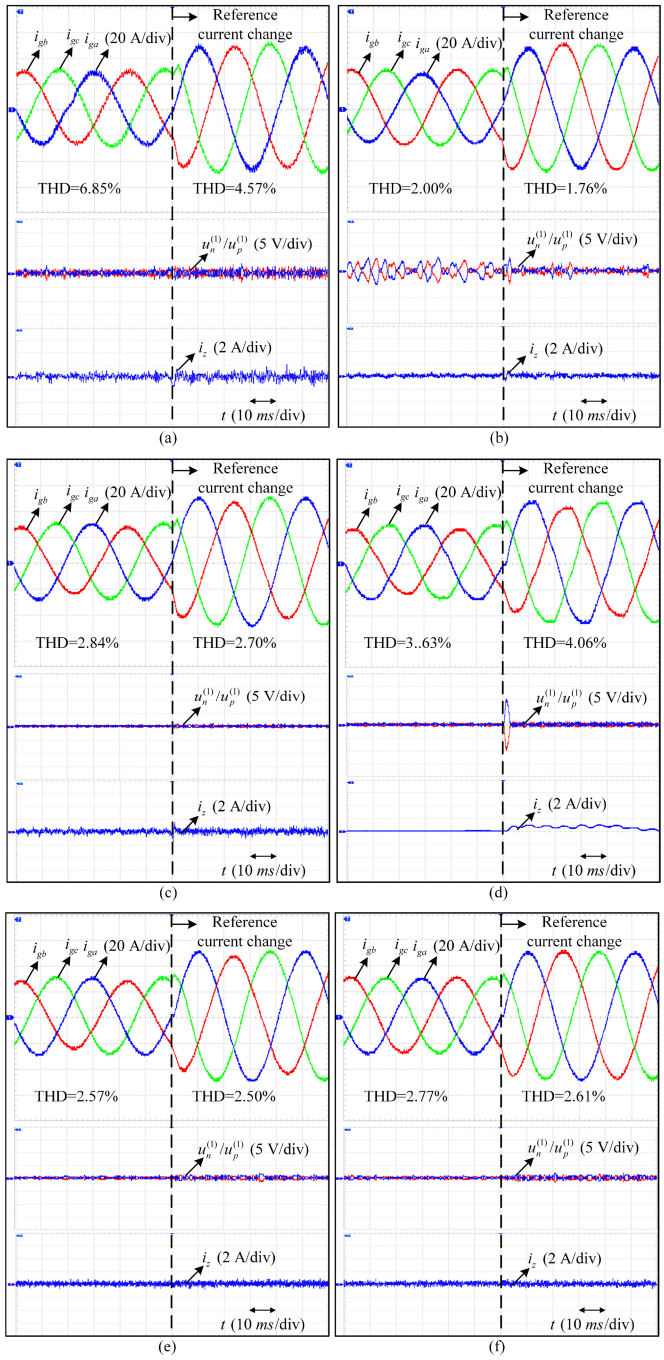

Fig. 14. Experiment comparison when the current reference value changed. (a) Conventional FCS-MPC. (b) ESO-MFPC. (c) ESO-SMFPC. (d) ESO-VV-MFPC. (e) ESO-P3L-SMFPC. (f) Proposed method.

C. Summary

Table V gives the comparison results among various MFPC methods. First, the proposed method can achieve high current quality and significantly improve the current tracking ability,

TABLE V
COMPARISON AMONG DIFFERENT MFPC METHODS

MFPC method	Robustness Performance				Reduction of switching frequency	Need known the dc-bus capacitances	Simplicity of weight selection	Calculation time
	Current quality	Current tracking ability	NP voltage suppression	ZSCC suppression				
ESO-MFPC	++	+	+	+	++	Yes	High	68 μs
ESO-SMFPC	++	+	+++	+	+	Yes	Low	62 μs
ESO-VV-MFPC	+	+	++	+++	+	Yes	Low	53 μs
ESO-P3L-MFPC	++	+	+++	++	+	No	Low	67 μs
Proposed method	++	+++	+++	++	+	No	Low	75 μs

Note: the more + indicates better performance.

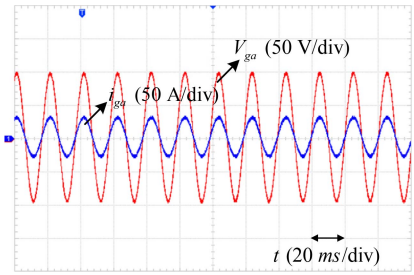

Fig. 15. Waveforms of the grid voltage and grid current with the proposed method.

indicating that NNO has better estimation ability than ESO. Second, the other two SMPC-based methods ensure the suppression and robustness of the NP voltage. On the contrary, the robustness of the NP voltage controlled by ESO-MFPC is poor because ESO-MFPC is based on the weighted cost function structure, as seen in (34). Moreover, the proposed method requires neither constructing the cost function for the NP voltage nor acquiring the value of dc-bus capacitances. Third, the proposed method is not as effective as ESO-VV-MFPC in suppressing ZSCC, because the latter uses only seven CVVs that can make CMV zero. However, the proposed method still has better inhibition effect compared with other methods. As for switching frequency, the ESO-MFPC has the smallest switching frequency, but at the expense of the worst NP voltage suppression effect. Finally, in addition to the parameter design of the observer, the proposed method only needs to design one weighting number m. The selection range of m is an integer from 2 to 6. In contrast, ESO-MFPC needs to design two weighting factors ($\lambda_{\text{np}}$and λ_z), whose selection range is all positive real numbers. However, in terms of computation time, the proposed method has limitations, because NNO has more computational burden than ESO algorithmically. It is suggested that FPGA + DSP dual-core system can be used to mitigate the computational burden.

VI. CONCLUSION

This article proposed a P3L-SMFPC method using NNO for the parallel-3LT^{2}C system. First, the cascaded SMPC proved inherently robust to filter parameters compared to weighted FCS-MPC. The proposed method further improves the robustness by designing the ULM of the grid-side currents and ZSCC and observing the uncertain terms with NNO, which shows better current tracking capability than ESO. On the other hand, the proposed NP voltage control method can not only avoid the continuous rise or fall of the NP voltage but also does not need to know the dc-bus capacitances. In addition, the proposed pseudo-three-layer structure dramatically simplifies the design of weight. Simulation and experiment results under mismatched filter parameters and different reference currents presented the performance evaluation. The findings show that the proposed method achieves excellent current quality and tracking ability with the NP voltage and ZSCC significantly inhibited. It is worth pointing out that the proposed method has some limitations in terms of computation time, and there are several parameters of NNO that need to be adjusted. In future studies, the simplification of parameter selection and algorithm complexity of NNO should be investigated.

REFERENCES

[1] A. Anthon, Z. Zhang, M. A. E. Andersen, D. G. Holmes, B. McGrath, and C. A. Teixeira, "The benefits of SiC MOSFETs in a T-type inverter for grid-tie applications," *IEEE Trans. Power Electron.*, vol. 32, no. 4, pp. 2808–2821, Apr. 2017.

[2] Z. Shao, X. Zhang, F. Wang, and R. Cao, "Modeling and elimination of zero-sequence circulating currents in parallel three-level T-type grid-connected inverters," *IEEE Trans. Power Electron.*, vol. 30, no. 2, pp. 1050–1063, Feb. 2015.

[3] C. Qin, C. Zhang, X. Xing, X. Li, A. Chen, and G. Zhang, "Simultaneous common-mode voltage reduction and neutral-point voltage balance scheme for the quasi-Z-source three-level T-type inverter," *IEEE Trans. Ind. Electron.*, vol. 67, no. 3, pp. 1956–1967, Mar. 2020.

[4] F. Wang, Y. Wang, Q. Gao, C. Wang, and Y. Liu, "A control strategy for suppressing circulating currents in parallel-connected PMSM drives with individual DC links," *IEEE Trans. Power Electron.*, vol. 31, no. 2, pp. 1680–1691, Feb. 2016.

[5] Z. Zeng, Z. Li, and S. M. Goetz, "A high performance interleaved discontinuous PWM strategy for two paralleled three-phase inverter," *IEEE Trans. Power Electron.*, vol. 35, no. 12, pp. 13042–13052, Dec. 2020.

[6] J. Zhou, J. O. Ojo, F. Tang, J. Haruna, and P. C. Loh, "A carrier-based discontinuous PWM for single and parallel three-level T-type converters with neutral-point potential balancing," *IEEE Trans. Ind. Appl.*, vol. 57, no. 5, pp. 5117–5127, Sep./Oct. 2021.

[7] W. Li et al., "Integrated modulation of dual-parallel three-level inverters with reduced common mode voltage and circulating current," *IEEE Trans. Power Electron.*, vol. 36, no. 11, pp. 13332–13344, Nov. 2021.

[8] J. Rodriguez et al., "Latest advances of model predictive control in electrical drives—Part I: Basic concepts and advanced strategies," *IEEE Trans. Power Electron.*, vol. 37, no. 4, pp. 3927–3942, Apr. 2022.

[9] X. Wang et al., "A novel model predictive control strategy to eliminate zero-sequence circulating current in paralleled three-level inverters," *IEEE J. Emerg. Sel. Topics Power Electron.*, vol. 7, no. 1, pp. 309–320, Mar. 2019.

[10] X. D. Wang, J. X. Zou, Y. Peng, C. Xie, K. Li, and J. M. G. Zapata, "Elimination of zero sequence circulating currents in paralleled three-level T-type inverters with a model predictive control strategy," *IET Power Electron*, vol. 11, no. 15, pp. 2573–2581, Dec. 2018.

[11] T. Jin, Y. Huang, Y. Lin, and M. N. D. Legrand, "Model predictive current control based on virtual voltage vector method for parallel three-level inverters," *IEEE J. Emerg. Sel. Topics Power Electron.*, vol. 9, no. 5, pp. 6049–6058, Oct. 2021.
[12] C. -K. Lin, J. -t. Yu, Y. -S. Lai, and H. -C. Yu, "Improved model-free predictive current control for synchronous reluctance motor drives," *IEEE Trans. Ind. Electron.*, vol. 63, no. 6, pp. 3942–3953, Jun. 2016.
[13] C. Ma, H. Li, X. Yao, Z. Zhang, and F. De Belie, "An improved model-free predictive current control with advanced current gradient updating mechanism," *IEEE Trans. Ind. Electron.*, vol. 68, no. 12, pp. 11968–11979, Dec. 2021.
[14] F. Yu, C. Zhou, X. Liu, and C. Zhu, "Model-free predictive current control for three-level inverter-fed IPMSM with an improved current difference updating technique," *IEEE Trans. Energy Convers.*, vol. 36, no. 4, pp. 3334–3343, Dec. 2021.
[15] B. Long, Z. Zhu, W. Yang, K. T. Chong, J. Rodríguez, and J. M. Guerrero, "Gradient descent optimization based parameter identification for FCS-MPC control of LCL-type grid connected converter," *IEEE Trans. Ind. Electron.*, vol. 69, no. 3, pp. 2631–2643, Mar. 2022.
[16] B. Long et al., "Moth–Flame-optimization-based parameter estimation for FCS-MPC-controlled grid-connected converter with LCL filter," *IEEE J. Emerg. Sel. Topics Power Electron.*, vol. 10, no. 4, pp. 4102–4114, Aug. 2022.
[17] Y. A. Zhou, H. M. Li, and H. G. Zhang, "Model-free deadbeat predictive current control of a surface-mounted permanent magnet synchronous motor drive system," *J. Power Electron.*, vol. 18, no. 1, pp. 103–115, Jan. 2018.
[18] Y. Zhang, J. Jin, and L. Huang, "Model-free predictive current control of PMSM drives based on extended State observer using ultralocal Model," *IEEE Trans. Ind. Electron.*, vol. 68, no. 2, pp. 993–1003, Feb. 2021.
[19] X. Liu, Y. Zhang, H. Yang, and J. Rodriguez, "Robust predictive current control of PWM rectifiers with LCL filters under unbalanced and distorted network conditions," *IET Power Electron*, vol. 15, no. 3, pp. 226–236, Feb. 2022.
[20] O. Babayomi and Z. Zhang, "Model-free predictive control of power converters with cascade-parallel extended State observers," *IEEE Trans. Ind. Electron.*, vol. 70, no. 10, pp. 10215–10226, Oct. 2023.
[21] X. Liu et al., "Neural predictor-based low switching frequency FCS-MPC for MMC with online weighting factors tuning," *IEEE Trans. Power Electron.*, vol. 37, no. 4, pp. 4065–4079, Apr. 2022.
[22] X. Liu et al., "Neural predictor-based dynamic surface predictive control for power converters," *IEEE Trans. Ind. Electron.*, vol. 70, no. 1, pp. 1057–1065, Jan. 2023.
[23] L. Cheng et al., "An improved data-driven based model predictive control for zero-sequence circulating current suppression in paralleled converters," *Int. J. Elect. Power.*, vol. 143, Dec. 2022, Art. no. 108401.
[24] L. Cheng, L. Qiu, W. Wu, X. Liu, J. Ma, and Y. Fang, "Virtual voltage vector-based sequential model-free predictive control for multiparalleled NPC inverters," *IEEE J. Emerg. Sel. Topics Power Electron.*, vol. 11, no. 3, pp. 3108–3116, Jun. 2023, doi: 10.1109/JESTPE.2023.3260299.
[25] M. Khalilzadeh, S. Vaez-Zadeh, J. Rodriguez, and R. Heydari, "Model-free predictive control of motor drives and power converters: A review," *IEEE Access*, vol. 9, pp. 105733–105747, 2021.
[26] M. Norambuena, J. Rodriguez, Z. Zhang, F. Wang, C. Garcia, and R. Kennel, "A very simple strategy for high-quality performance of AC machines using model predictive control," *IEEE Trans. Power Electron.*, vol. 34, no. 1, pp. 794–800, Jan. 2019.
[27] K. Zhang et al., "Tolerant sequential model predictive direct torque control of permanent magnet synchronous machine drives," *IEEE Trans. Transp. Electr.*, vol. 6, no. 3, pp. 1167–1176, Sep. 2020.
[28] Y. Zhang, B. Zhang, H. Yang, M. Norambuena, and J. Rodriguez, "Generalized sequential model predictive control of IM drives with field-weakening ability," *IEEE Trans. Power Electron.*, vol. 34, no. 9, pp. 8944–8955, Sep. 2019.
[29] B. Long, T. Cao, D. Sheng, J. Rodriguez, J. M. Guerrero, and K. T. Chong, "Sequential model predictive fault-tolerance control for T-type three-level grid-connected converters with LCL filters," *IEEE Trans. Ind. Electron.*, vol. 69, no. 9, pp. 9039–9051, Sep. 2022.
[30] B. Long et al., "Noninteger lexicographic-optimization-based sequential model-predictive fault-tolerant control of T-type shunt active power filter," *IEEE Trans. Power Electron.*, vol. 37, no. 6, pp. 7169–7184, Jun. 2022.
[31] B. Long, T. Cao, D. Shen, J. M. Guerrero, J. Rodríguez, and K. T. Chong, "Fault-tolerant sequential MPC for vertical switch open-circuit Fault and ZSCC suppression for parallel T-type converters," *IEEE Trans. Power Electron.*, vol. 37, no. 10, pp. 11787–11802, Oct. 2022.
[32] Y. Yang, H. Wen, M. Fan, M. Xie, and R. Chen, "Fast finite-switching-State model predictive control method without weighting factors for T-type three-level three-phase inverters," *IEEE Trans. Ind. Inform.*, vol. 15, no. 3, pp. 1298–1310, Mar. 2019.

Tianxu Cao (Student Member, IEEE) received the B.S. and M.S. degrees in electrical engineering from the University of Electronic Science and Technology of China, Chengdu, China, in 2020 and 2023. He is currently working toward the Ph.D. degree in electrical engineering with the Technical University of Munich, Munich, Germany.

His current research interest includes wide-band gap semiconductor devices, loss modeling of power converters, fault-tolerant control of power converters, model predictive control, fractional-order systems, reliability of power electronic system, and so on.

YinHui Yu received the B.S and M.Sc. degrees from the Chongqing University, Chongqing, China in 2006 and 2009, respectively, both in electrical engineering.

Since 2009, he has been with China Nuclear Power Technology Research Institute Company Ltd., Shenzhen, China. His current research interesting include the optimization of the Nuclear Power and stored energy, involving virtual inertia control, fault-tolerant control of power converters, reliability of micro-grids and power electronic systems, and so on.

Jiahao Zhang received the B.S. degree in electrical engineering and automation from the Taiyuan University of Technology, Taiyuan, China, in 2021. He is currently working toward the M.S degree in electronic information with the University of Electronic Science and Technology of China, Chengdu, China.

His current research interests include model predictive control of paralleled converters, adaptive droop control, model-free predictive control, parameter robustness of power electronic systems, and so on.

Jose Rodriguez (Life Fellow, IEEE) received the Engineer degree in electrical engineering from the Universidad Tecnica Federico Santa Maria, Valparaiso, Chile, in 1977 and the Dr.-Ing. degree in electrical engineering from the University of Erlangen, Erlangen, Germany, in 1985.

Since 1977, he has been with the Department of Electronics Engineering, Universidad Tecnica Federico Santa Maria, where he was a Full Professor and the President. Since 2015, he has been the President, and since 2019, he has been a Full Professor with Universidad Andres Bello in Santiago, Chile. He has coauthored 2 books, several book chapters and more than 400 journal and conference papers. His main research interests include multilevel inverters, new converter topologies, control of power converters, and adjustable-speed drives.

Dr. Rodriguez is Member of the Chilean Academy of Engineering. He was the recipient of number of best paper awards from journals of the IEEE. In 2014, he was the recipient of the National Award of Applied Sciences and Technology from the government of Chile and the Eugene Mittelmann Award from the Industrial Electronics Society of the IEEE in 2015. In years 2014 to 2020, he has been included in the list of Highly Cited Researchers published by Web of Science.

Kil To Chong (Member, IEEE) received the Ph.D. degree in mechanical engineering from Texas A&M University, College Station, TX, USA, in 1995.

He is currently a Professor and the Department Head of the School of Electronics and Information Engineering and a Member and the Head of the Advanced Electronics and Information Research Center, Chonbuk National University, Jeonju, South Korea. His research interests include motor fault detection and control, network system control, sensor network systems, time-delay systems, and neural networks.

Bo Long (Senior Member, IEEE) received the B.S. degree in electrical engineering from the Xi'an Petroleum University, Xian, China, in 2001, and the Ph.D. degree in electrical engineering from Xian Jiaotong University, Shanxi, China, in 2008.

He was with the Department of Power Electronics, School of Mechatronics Engineering, University of Electronic Science and Technology of China (UESTC), in 2008, and has been an Associate Professor since 2014. From 2017 to 2018, he was a Visiting Scholar (Guest Post-Doctoral Researcher) in the area of renewable energy and microgrids with the Department of Electrical Engineering, Tsinghua University, Beijing, China. He has authored more than 20 SCIE-indexed journal papers and one book chapter in the area of power electronics, motor control, battery management system, and smart grid. He has seven issued and ten pending patents. He is currently the Supervisor for 11 master students, two of which have been nominated as provincial outstanding graduate student of UESTC. His research interests include ac/dc microgrids, grid-connected converters for renewable energy systems and DGs, model predictive control, power quality, multilevel converters, ac motor control, and resonance suppression technique for smart grid applications.

He is an Active Reviewer for IEEE TRANSACTIONS ON POWER ELECTRONICS, *ISA Transactions*, *Applied Energy, Energy*, IEEE TRANSACTIONS ON SMART GRID, IEEE TRANSACTIONS ON INDUSTRIAL ELECTRONICS, IEEE TRANSACTIONS ON SUSTAINABLE ENERGY, and IEEE TRANSACTIONS ON ENERGY CONVERSION.